A Decomposed Two-Port Network Impedance Modeling Method of Type-3 Wind Generation System with Grid-Forming Control

Huang, Liang; Wu, Chao; Zhou, Dao; Blaabjerg, Frede; Boldea, Ion; He, Shan

Published in:
Proceedings of the 2023 IEEE Energy Conversion Congress and Exposition (ECCE)

DOI (link to publication from Publisher):
10.1109/ECCE53617.2023.10362378

Publication date:
2023

Document Version
Accepted author manuscript, peer reviewed version

A Decomposed Two-Port Network Impedance Modeling Method of Type-3 Wind Generation System with Grid-Forming Control

Liang Huang
AAU Energy
Aalborg University
Aalborg, Denmark
lihu@energy.aau.dk

Chao Wu
Electrical Engineering
Shanghai Jiao Tong University
Shanghai, China
wuchao@sjtu.edu.cn

Dao Zhou
AAU Energy
Aalborg University
Aalborg, Denmark
zda@energy.aau.dk

Frede Blaabjerg
AAU Energy
Aalborg University
Aalborg, Denmark
fbl@energy.aau.dk

Ion Boldea
Electrical Engineering
Politehnica University of Timisoara
Timisoara, Romania
ion.boldea@upt.ro

Shan He
AAU Energy
Aalborg University
Aalborg, Denmark
she@energy.aau.dk

***Abstract*—The doubly-fed induction generator (DFIG) has been widely used in the field of wind generation. However, due to the couplings on both dc-side and ac-side, the full-order small-signal impedance model of the DFIG system is hard to build. To solve this problem, this paper proposes a decomposed two-port network impedance modeling method. With this method, the total admittance of the DFIG system is decomposed into four components, and each of them can be calculated independently. Then, a full-order small-signal admittance model can be obtained accordingly. The proposed modeling method has three main advantages: 1) high accuracy; 2) low complexity of the modeling process; 3) the impact of the dc-link coupling can be analyzed intuitively. Finally, this paper provides the ac terminal admittance calculation and measurement results of the DFIG system with grid-forming control for cross-validation.**

Keywords—double-fed induction generator, impedance model, dc-link coupling, two-port network, grid-forming control

I. INTRODUCTION

As the penetration of wind energy increases, conventional wind generators with grid-following (GFL) control may not fully meet grid code requirements to keep voltage and frequency stability [1]. Hence, grid-forming (GFM) control technology is deemed to be a promising solution for future low-inertia power systems, because it can inherit the voltage source characteristics of synchronous generators (SGs) [2]-[4]. To ensure wind generators can operate stably in power systems, small-signal modeling and stability analysis are key tools to design a stable and robust wind generator system [5].

Currently, Type-3 and Type-4 wind generators are two mainstream types of wind generators [6]. Compared with Type-4 wind generators, Type-3 wind generators have the advantage of lower cost, so they have been widely used in on-shore wind power plants [7]-[10]. For the Type-3 wind generator, the doubly-fed induction generator (DFIG) and the back-to-back converters are connected on both rotor-side and stator-side, so the DFIG stator currents and the grid-side converter (GSC) output currents are influenced by each other. This physical coupling effect makes it difficult to derive the full-order impedance model of the Type-3 wind generators. A conventional modeling method is assuming a constant dc-link voltage by ignoring the dc-link coupling, so that the rotor-side converter (RSC) and the GSC can be modeled separately [11]-[13]. However, the obtained model is not a full-order model, and it lacks accuracy in the low-frequency region. Moreover, to build a full-order impedance model, some improved modeling methods have been proposed [14], [15]. In [14], a full-order impedance model is derived by combining two three-port modules of the GSC and RSC. In [15], a full-order sequence impedance modeling method based on voltage perturbations and current responses is introduced. However, these modeling methods are still too complicated to show physical insights, and impact of the dc-link coupling has not been revealed clearly.

Different from existing methods, this paper proposes a novel decomposed two-port network impedance modeling method for the Type-3 wind generator. With this method, the physically coupled DFIG system can be decomposed into four subsystems and it can be modeled by a 2×2 matrix. Thus, the admittance models of the RSC and the GSC can be represented by the diagonal elements of the matrix, while the dc-link coupling between the RSC and the GSC is able to be reflected by the non-diagonal elements. Each of the four elements in the 2×2 matrix can be calculated independently. Then, a full-order admittance model can be obtained by adding the four elements. The proposed modeling method can be used for Type-3 wind generators with either GFL or GFM control. In this paper, Type-3 wind generators with GFM control are chosen as an example for analysis to show the effectiveness of the proposed method.

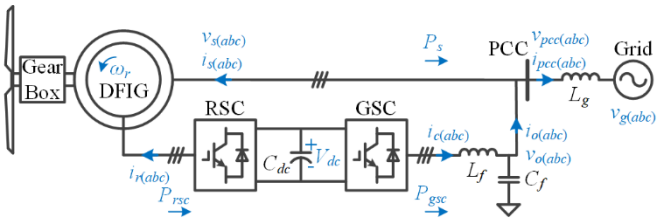

(a) Physical configuration of Type-3 wind generation system

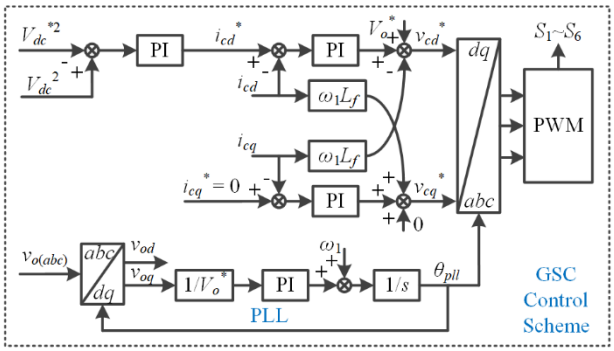

(b) PLL-based dc voltage control scheme on the GSC

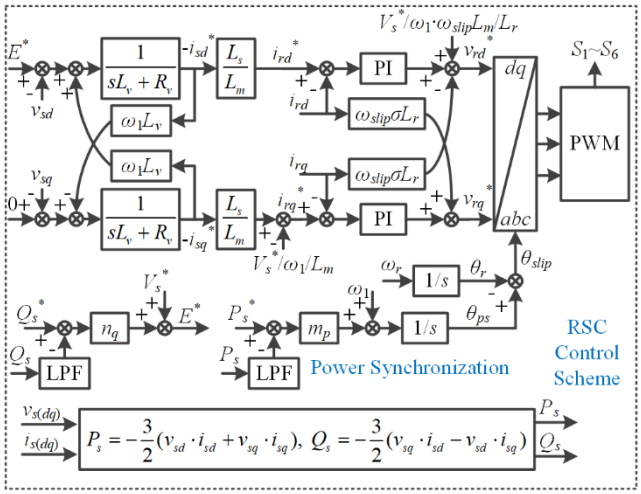

(c) Virtual-admittance-based GFM control scheme on the RSC

Fig. 1. Typical GFM control scheme for Type-3 wind generation systems.

The rest of this paper is organized as follows. Section II introduces a typical Type-3 wind generation system with grid-forming control, which is selected in this paper for study. Section III introduces a new two-port network-based decomposed impedance modeling method. Then, the calculated results and frequency scanning results of the terminal admittance by simulation are presented in Section IV. Finally, this paper is concluded in Section V.

II. Study System

A. Configurations of Typical Grid-Forming Control Scheme for Type-3 Wind Generation System

The physical configuration of Type-3 wind generation system is shown in Fig. 1(a), which includes a DFIG, an RSC, and a GSC. The reference directions of all variables are defined in Fig. 1(a). Besides, the detailed control schemes of the GSC and RSC are presented in Fig. 1(b) and (c), respectively.

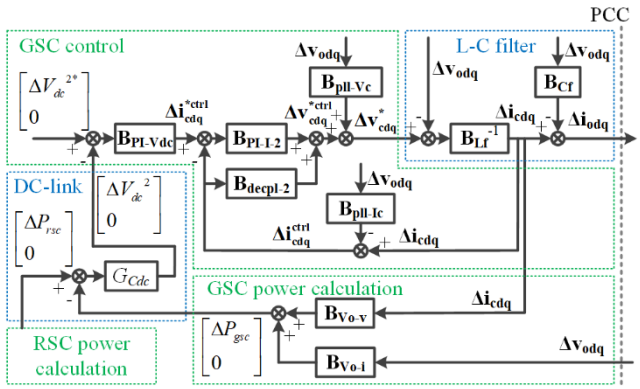

(a) Small-signal d-q impedance model of GSC

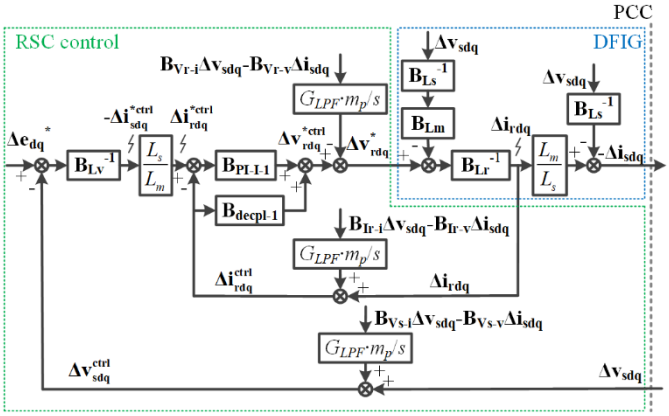

(b) Small-signal d-q impedance model of RSC+DFIG

Fig. 2. Small-signal impedance model of GSC and RSC+DFIG.

Fig. 1(b) shows a typical PLL-based dc voltage control scheme on the GSC [16], which includes an inner current control loop, a dc voltage control loop, and a PLL.

Moreover, Fig. 1(c) shows a typical virtual-admittance-based GFM control scheme on the RSC [5], where an inner current control loop, an outer voltage control loop, and a power synchronization control loop are included.

As shown in Fig. 1, the Type-3 wind generator can be divided into two subsystems (i.e., the RSC-side subsystem and GSC-side subsystem). The small-signal impedance models of two subsystems in the frequency domain are modeled in Fig. 2, where the symbol **B** represents a 2×2 matrix, and the symbol G represents a transfer function (See the Appendix). Since the dc-link voltage is controlled by the GSC, the model of the dc-link is included in the GSC-side subsystem, as shown in Fig. 2(a). Besides, considering the DFIG is controlled by the RSC, the model of the DFIG is included in the RSC-side subsystem, as shown in Fig. 2(b). Then, modeling methods of the whole system will be introduced in the following section.

III. Proposed Decomposed Two-Port Network Impedance Modeling Method

Since the GSC and the RSC are coupled on both dc-side and ac-side in the DFIG system, it is hard to derive its full-order small-signal impedance model. In this section, port network analysis will be used to solve this problem.

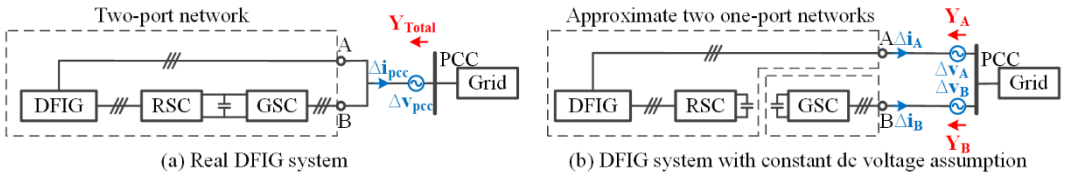

Fig. 3. Conventional approximate impedance modeling method for the DFIG system ($\mathbf{Y}_{\mathbf{Total}} \approx \mathbf{Y}_{\mathbf{A}} + \mathbf{Y}_{\mathbf{B}}$).

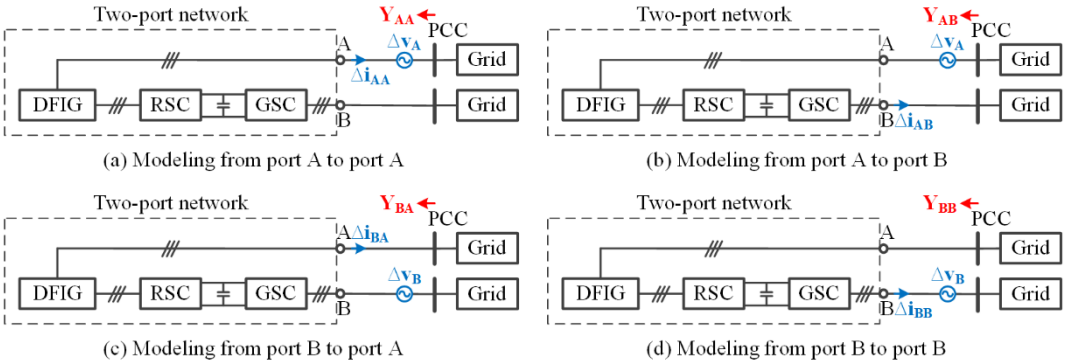

Fig. 4. Proposed two-port-network-based full-order impedance modeling method ($\mathbf{Y}_{\mathbf{Total}} = \mathbf{Y}_{\mathbf{AA}} + \mathbf{Y}_{\mathbf{AB}} + \mathbf{Y}_{\mathbf{BA}} + \mathbf{Y}_{\mathbf{BB}}$).

A. Conventional Impedance Modeling Method of DFIG System by Ignoring DC-link Voltage Dynamics

As presented in Fig. 3(a), the real DFIG system can be represented by a two-port network. When injecting a small-signal voltage perturbation $\Delta\mathbf{v}_{\mathbf{pcc}}$ at the point of common coupling (PCC), there is a small-signal current response $\Delta\mathbf{i}_{\mathbf{pcc}}$ at the PCC. Thus, the total ac terminal admittance $\mathbf{Y}_{\mathbf{Total}}$ of the DFIG system can be obtained according to $\Delta\mathbf{v}_{\mathbf{pcc}}$ and $\Delta\mathbf{i}_{\mathbf{pcc}}$. However, due to the coupling between port A and port B, it is hard to derive the analytical expression of $\mathbf{Y}_{\mathbf{Total}}$. To overcome this difficulty, a conventional impedance modeling method is shown in Fig. 3(b), where the dc-link voltage is assumed to be constant [11]-[13]. Thus, the original two-port network can be separated into two one-port networks, and each one-port network can be modeled easily. However, the obtained model is not a full-order model, and part of the accuracy is lost by using this approximate method.

B. Proposed Decomposed Impedance Modeling Method

Different from existing modeling methods, a decomposed two-port network impedance modeling method for the DFIG system is proposed in this paper, as shown in Fig. 4, where the ac-side of the DFIG system is decoupled. Port A and port B are connected to two identical grids, respectively. Thus, the four admittance components $\mathbf{Y}_{\mathbf{AA}}$, $\mathbf{Y}_{\mathbf{AB}}$, $\mathbf{Y}_{\mathbf{BA}}$, and $\mathbf{Y}_{\mathbf{BB}}$ of the two-port network can be derived separately. The relationship between the total ac terminal admittance $\mathbf{Y}_{\mathbf{Total}}$ and the four admittance components is given by (1). The detailed expressions of $\mathbf{Y}_{\mathbf{AA}}$, $\mathbf{Y}_{\mathbf{AB}}$, $\mathbf{Y}_{\mathbf{BA}}$, and $\mathbf{Y}_{\mathbf{BB}}$ will be introduced as follows.

$$\mathbf{Y}_{\mathbf{Total}} = \frac{-\Delta\mathbf{i}_{\mathbf{pcc}}}{\Delta\mathbf{v}_{\mathbf{pcc}}} = \frac{-(\Delta\mathbf{i}_{\mathbf{AA}} + \Delta\mathbf{i}_{\mathbf{AB}} + \Delta\mathbf{i}_{\mathbf{BA}} + \Delta\mathbf{i}_{\mathbf{BB}})}{\Delta\mathbf{v}_{\mathbf{pcc}}} = \mathbf{Y}_{\mathbf{AA}} + \mathbf{Y}_{\mathbf{AB}} + \mathbf{Y}_{\mathbf{BA}} + \mathbf{Y}_{\mathbf{BB}} \tag{1}$$

As shown in Fig. 4(a), when small-signal voltage perturbation $\Delta\mathbf{v}_{\mathbf{A}}$ is injected into the two-port network system from port A, there is a current response $\Delta\mathbf{i}_{\mathbf{AA}}$ at port A. Thus, the admittance $\mathbf{Y}_{\mathbf{AA}}$ can be derived as:

$$\mathbf{Y}_{\mathbf{AA}}^{\mathbf{dq}}(s) = \frac{-\Delta\mathbf{i}_{\mathbf{AA}}^{\mathbf{dq}}(s)}{\Delta\mathbf{v}_{\mathbf{A}}^{\mathbf{dq}}(s)} = \frac{\Delta\mathbf{i}_{\mathbf{sdq}}(s)}{\Delta\mathbf{v}_{\mathbf{sdq}}(s)} \tag{2}$$

where $\Delta\mathbf{i}_{\mathbf{sdq}}$ and $\Delta\mathbf{v}_{\mathbf{sdq}}$ are the stator current and stator voltage.

According to Fig. 2(b), the admittance $\mathbf{Y}_{\mathbf{AA}}$ in (2) can be deduced as:

$$\begin{aligned}\mathbf{Y}_{\mathbf{AA}}^{\mathbf{dq}}(s) = &\{\frac{L_s}{L_m}(\mathbf{B}_{\mathbf{Lr}} + \mathbf{B}_{\mathbf{PI\text{-}I\text{-}1}} - \mathbf{B}_{\mathbf{decpl\text{-}1}}) + G_{LPF}\cdot\frac{m_p}{s}\\ &\cdot[\mathbf{B}_{\mathbf{Vr\text{-}v}} + (\mathbf{B}_{\mathbf{PI\text{-}I\text{-}1}} - \mathbf{B}_{\mathbf{decpl\text{-}1}})\cdot\mathbf{B}_{\mathbf{Ir\text{-}v}} + \frac{L_s}{L_m}\cdot\mathbf{B}_{\mathbf{PI\text{-}I\text{-}1}}\cdot\mathbf{B}_{\mathbf{Lr}}^{-1}\\ &\cdot\mathbf{B}_{\mathbf{Vs\text{-}v}}]\}^{-1}\cdot\{\mathbf{B}_{\mathbf{Lm}}\mathbf{B}_{\mathbf{Ls}}^{-1} + \frac{L_s}{L_m}\cdot\mathbf{B}_{\mathbf{PI\text{-}I\text{-}1}}\cdot\mathbf{B}_{\mathbf{Lv}}^{-1} + \frac{L_s}{L_m}(\mathbf{B}_{\mathbf{Lr}}\\ &+\mathbf{B}_{\mathbf{PI\text{-}I\text{-}1}} - \mathbf{B}_{\mathbf{decpl\text{-}1}})\cdot\mathbf{B}_{\mathbf{Ls}}^{-1} + G_{LPF}\cdot\frac{m_p}{s}\cdot[\mathbf{B}_{\mathbf{Vr\text{-}i}} + (\mathbf{B}_{\mathbf{PI\text{-}I\text{-}1}}\\ &-\mathbf{B}_{\mathbf{decpl\text{-}1}})\cdot\mathbf{B}_{\mathbf{Ir\text{-}i}} + \frac{L_s}{L_m}\cdot\mathbf{B}_{\mathbf{PI\text{-}I\text{-}1}}\cdot\mathbf{B}_{\mathbf{Lv}}^{-1}\cdot\mathbf{B}_{\mathbf{Vs\text{-}i}}]\}\end{aligned} \tag{3}$$

where the detailed expressions of the matrixes are listed in (A1) - (A12) in the Appendix.

Moreover, as shown in Fig. 4(b), when small-signal voltage perturbation $\Delta\mathbf{v}_{\mathbf{A}}$ is injected into the two-port network system from port A, there is a current response $\Delta\mathbf{i}_{\mathbf{AB}}$ at port B due to the dc-link coupling. Hence, the admittance $\mathbf{Y}_{\mathbf{AB}}$ can be expressed as (4).

$$\mathbf{Y}_{\mathbf{AB}}^{\mathbf{dq}}(s)=\frac{-\Delta\mathbf{i}_{\mathbf{AB}}^{\mathbf{dq}}(s)}{\Delta\mathbf{v}_{\mathbf{A}}^{\mathbf{dq}}(s)}=\frac{-\Delta\mathbf{i}_{\mathbf{odq}}(s)}{\Delta\mathbf{v}_{\mathbf{sdq}}(s)} \tag{4}$$

where $\Delta\mathbf{i}_{\mathbf{odq}}$ is the output current of the GSC and $\Delta\mathbf{v}_{\mathbf{sdq}}$ is the stator voltage of the DFIG.

In Fig. 2(a), assuming that $\Delta\mathbf{v}_{\mathbf{odq}}$ is equal to zero, the transfer function from ΔP_{rsc} to $\Delta\mathbf{i}_{\mathbf{odq}}$ can be deduced as:

$$\begin{aligned}\Delta\mathbf{i}_{\mathbf{odq}}(s)=&-(\mathbf{B}_{\mathbf{Lf}}+\mathbf{B}_{\mathbf{PI\text{-}I\text{-}2}}-\mathbf{B}_{\mathbf{PI\text{-}I\text{-}2}}\mathbf{B}_{\mathbf{PI\text{-}Vdc}}G_{Cdc}\mathbf{B}_{\mathbf{Vo\text{-}v}}\\&-\mathbf{B}_{\mathbf{decpl\text{-}2}})^{-1}\cdot(\mathbf{B}_{\mathbf{PI\text{-}I\text{-}2}}\mathbf{B}_{\mathbf{PI\text{-}Vdc}}G_{Cdc})\cdot\begin{bmatrix}\Delta P_{rsc}\\0\end{bmatrix}\end{aligned} \tag{5}$$

Since the output power of the RSC is basically the same as the output power of the DFIG on the rotor side, the small-signal expression of the power ΔP_{rsc} is given by (6).

$$\begin{bmatrix}\Delta P_{rsc}\\0\end{bmatrix}=-\frac{3}{2}\cdot\left\{\begin{bmatrix}i_{rd0}&i_{rq0}\\0&0\end{bmatrix}\cdot\begin{bmatrix}\Delta v_{rd}\\\Delta v_{rq}\end{bmatrix}+\begin{bmatrix}v_{rd0}&v_{rq0}\\0&0\end{bmatrix}\cdot\begin{bmatrix}\Delta i_{rd}\\\Delta i_{rq}\end{bmatrix}\right\} \tag{6}$$

where subscript '$_0$' represents steady-state operating points.

Then, according to the stator/rotor voltage and flux expressions of the DFIG system listed in (7), the power ΔP_{rsc} in (6) can be derived as (8).

$$\begin{cases}v_{rd}=R_r i_{rd}+s\psi_{rd}-\omega_{slip}\psi_{rq}\\v_{rq}=R_r i_{rq}+s\psi_{rq}+\omega_{slip}\psi_{rd}\\\psi_{sd}=L_s i_{sd}+L_m i_{rd}\\\psi_{sq}=L_s i_{sq}+L_m i_{rq}\\\psi_{rd}=L_r i_{rd}+L_m i_{sd}\\\psi_{rq}=L_r i_{rq}+L_m i_{sq}\end{cases} \tag{7}$$

$$\begin{aligned}\begin{bmatrix}\Delta P_{rsc}\\0\end{bmatrix}=&-\frac{3}{2}\cdot\left\{\left[\frac{(L_m{}^2-L_sL_r)s-2R_rL_s}{L_m}\cdot\begin{bmatrix}i_{rd0}&i_{rq0}\\0&0\end{bmatrix}\right.\right.\\&\left.-\frac{\omega_{slip}}{\omega_1}\cdot\begin{bmatrix}v_{sd0}&v_{sq0}\\0&0\end{bmatrix}\right]\cdot\begin{bmatrix}\Delta i_{sd}\\\Delta i_{sq}\end{bmatrix}+\left[\frac{L_rs+2R_r}{L_m}\cdot\begin{bmatrix}i_{rd0}&i_{rq0}\\0&0\end{bmatrix}\right.\\&\left.\left.+\omega_{slip}\cdot\begin{bmatrix}-i_{sq0}&i_{sd0}\\0&0\end{bmatrix}\right]\cdot\begin{bmatrix}s&-\omega_1\\\omega_1&s\end{bmatrix}^{-1}\cdot\begin{bmatrix}\Delta v_{sd}\\\Delta v_{sq}\end{bmatrix}\right\}\end{aligned} \tag{8}$$

It can be seen from (2) that $\Delta\mathbf{i}_{\mathbf{sdq}}$ can be expressed by "$\mathbf{Y}_{\mathbf{AA}}\cdot\Delta\mathbf{v}_{\mathbf{sdq}}$". So, (8) can be derived as (9).

$$\begin{aligned}\begin{bmatrix}\Delta P_{rsc}\\0\end{bmatrix}=&-\frac{3}{2}\cdot\left\{\left[\frac{(L_m{}^2-L_sL_r)s-2R_rL_s}{L_m}\cdot\begin{bmatrix}i_{rd0}&i_{rq0}\\0&0\end{bmatrix}\right.\right.\\&\left.-\frac{\omega_{slip}}{\omega_1}\cdot\begin{bmatrix}v_{sd0}&v_{sq0}\\0&0\end{bmatrix}\right]\cdot\mathbf{Y}_{\mathbf{AA}}^{\mathbf{dq}}(s)+\left[\frac{L_rs+2R_r}{L_m}\cdot\begin{bmatrix}i_{rd0}&i_{rq0}\\0&0\end{bmatrix}\right.\\&\left.\left.+\omega_{slip}\cdot\begin{bmatrix}-i_{sq0}&i_{sd0}\\0&0\end{bmatrix}\right]\cdot\begin{bmatrix}s&-\omega_1\\\omega_1&s\end{bmatrix}^{-1}\right\}\cdot\Delta\mathbf{v}_{\mathbf{sdq}}(s)\end{aligned} \tag{9}$$

Substituting (5) and (9) into (4), the admittance $\mathbf{Y}_{\mathbf{AB}}$ can be deduced as:

$$\begin{aligned}\mathbf{Y}_{\mathbf{AB}}^{\mathbf{dq}}(s)=&\frac{-3}{2}\cdot(\mathbf{B}_{\mathbf{Lf}}+\mathbf{B}_{\mathbf{PI\text{-}I\text{-}2}}-\mathbf{B}_{\mathbf{PI\text{-}I\text{-}2}}\mathbf{B}_{\mathbf{PI\text{-}Vdc}}G_{Cdc}\mathbf{B}_{\mathbf{Vo\text{-}v}}\\&-\mathbf{B}_{\mathbf{decpl\text{-}2}})^{-1}\cdot(\mathbf{B}_{\mathbf{PI\text{-}I\text{-}2}}\mathbf{B}_{\mathbf{PI\text{-}Vdc}}G_{Cdc})\cdot\{[\frac{(L_m{}^2-L_sL_r)s-2R_rL_s}{L_m}\\&\cdot\begin{bmatrix}i_{rd0}&i_{rq0}\\0&0\end{bmatrix}-\frac{\omega_{slip}}{\omega_1}\cdot\begin{bmatrix}v_{sd0}&v_{sq0}\\0&0\end{bmatrix}]\cdot\mathbf{Y}_{\mathbf{AA}}^{\mathbf{dq}}(s)+[\frac{L_rs+2R_r}{L_m}\\&\cdot\begin{bmatrix}i_{rd0}&i_{rq0}\\0&0\end{bmatrix}+\omega_{slip}\cdot\begin{bmatrix}-i_{sq0}&i_{sd0}\\0&0\end{bmatrix}]\cdot\begin{bmatrix}s&-\omega_1\\\omega_1&s\end{bmatrix}^{-1}\}\end{aligned} \tag{10}$$

where the detailed expressions of the matrixes are listed in (A13) - (A18) in the Appendix.

In addition, as presented in Fig. 4(c), when small-signal voltage perturbation $\Delta\mathbf{v}_{\mathbf{B}}$ is injected into the two-port network system from port B, there is a current response $\Delta\mathbf{i}_{\mathbf{BA}}$ at port A. So, the admittance $\mathbf{Y}_{\mathbf{BA}}$ can be expressed as:

$$\mathbf{Y}_{\mathbf{BA}}^{\mathbf{dq}}(s)=\frac{-\Delta\mathbf{i}_{\mathbf{BA}}^{\mathbf{dq}}(s)}{\Delta\mathbf{v}_{\mathbf{B}}^{\mathbf{dq}}(s)}=\frac{\Delta\mathbf{i}_{\mathbf{sdq}}(s)}{\Delta\mathbf{v}_{\mathbf{odq}}(s)} \tag{11}$$

where $\Delta\mathbf{v}_{\mathbf{odq}}$ is the output voltage of the GSC, and $\Delta\mathbf{i}_{\mathbf{sdq}}$ is the stator current of the DFIG.

Since the measured value of dc-link voltage is used for the voltage modulation on the RSC, the output voltage of the RSC is independent from the dc-link voltage. Hence, the injected small-signal perturbation at port B can only be transferred to the dc-link, but it cannot be transferred to port A. So, $\Delta\mathbf{i}_{\mathbf{BA}}$ is equal to zero and the admittance $\mathbf{Y}_{\mathbf{BA}}$ can be deduced as:

$$\mathbf{Y}_{\mathbf{BA}}^{\mathbf{dq}}(s)=\frac{\mathbf{0}}{\Delta\mathbf{v}_{\mathbf{B}}^{\mathbf{dq}}(s)}=\mathbf{0} \tag{12}$$

Furthermore, as presented in Fig. 4(d), when small-signal voltage perturbation $\Delta\mathbf{v}_{\mathbf{B}}$ is injected into the two-port network system from port B, there is a current response $\Delta\mathbf{i}_{\mathbf{BB}}$ at port B. Thus, the admittance $\mathbf{Y}_{\mathbf{BB}}$ can be given by (13).

$$\mathbf{Y}_{\mathbf{BB}}^{\mathbf{dq}}(s)=\frac{-\Delta\mathbf{i}_{\mathbf{BB}}^{\mathbf{dq}}(s)}{\Delta\mathbf{v}_{\mathbf{B}}^{\mathbf{dq}}(s)}=\frac{-\Delta\mathbf{i}_{\mathbf{odq}}(s)}{\Delta\mathbf{v}_{\mathbf{odq}}(s)} \tag{13}$$

where $\Delta\mathbf{v}_{\mathbf{odq}}$ and $\Delta\mathbf{i}_{\mathbf{odq}}$ are the voltage and current of the GSC.

In Fig. 2(a), assuming that ΔP_{rsc} is equal to zero, the transfer function from $\Delta\mathbf{v}_{\mathbf{odq}}$ to $\Delta\mathbf{i}_{\mathbf{odq}}$ can be deduced as:

$$\begin{aligned}\Delta\mathbf{i}_{\mathbf{odq}}(s)=&-(\mathbf{B}_{\mathbf{Lf}}+\mathbf{B}_{\mathbf{PI\text{-}I\text{-}2}}-\mathbf{B}_{\mathbf{PI\text{-}I\text{-}2}}\mathbf{B}_{\mathbf{PI\text{-}Vdc}}G_{Cdc}\mathbf{B}_{\mathbf{Vo\text{-}v}}\\&-\mathbf{B}_{\mathbf{decpl\text{-}2}})^{-1}\cdot[\mathbf{I}-(\mathbf{B}_{\mathbf{PI\text{-}I\text{-}2}}-\mathbf{B}_{\mathbf{decpl\text{-}2}})\mathbf{B}_{\mathbf{pll\text{-}Ic}}-\mathbf{B}_{\mathbf{pll\text{-}Vc}}\\&-\mathbf{B}_{\mathbf{PI\text{-}I\text{-}2}}\mathbf{B}_{\mathbf{PI\text{-}Vdc}}G_{Cdc}\mathbf{B}_{\mathbf{Vo\text{-}i}}]\cdot\Delta\mathbf{v}_{\mathbf{odq}}(s)-\mathbf{B}_{\mathbf{Cf}}\cdot\Delta\mathbf{v}_{\mathbf{odq}}(s)\end{aligned} \tag{14}$$

Substituting (14) into (13), $\mathbf{Y}_{\mathbf{BB}}$ can be derived by (15).

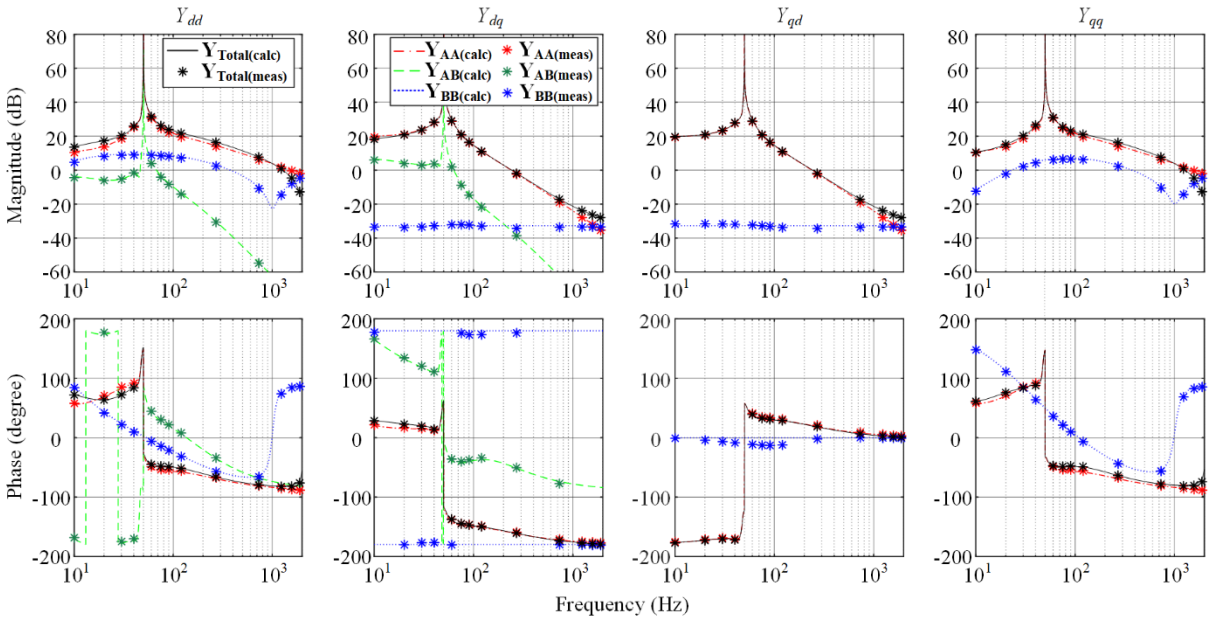

Fig. 5. Admittance measurement results of a GFM Type-3 wind generator under sub-synchronous speed (ω_r = 40 Hz).

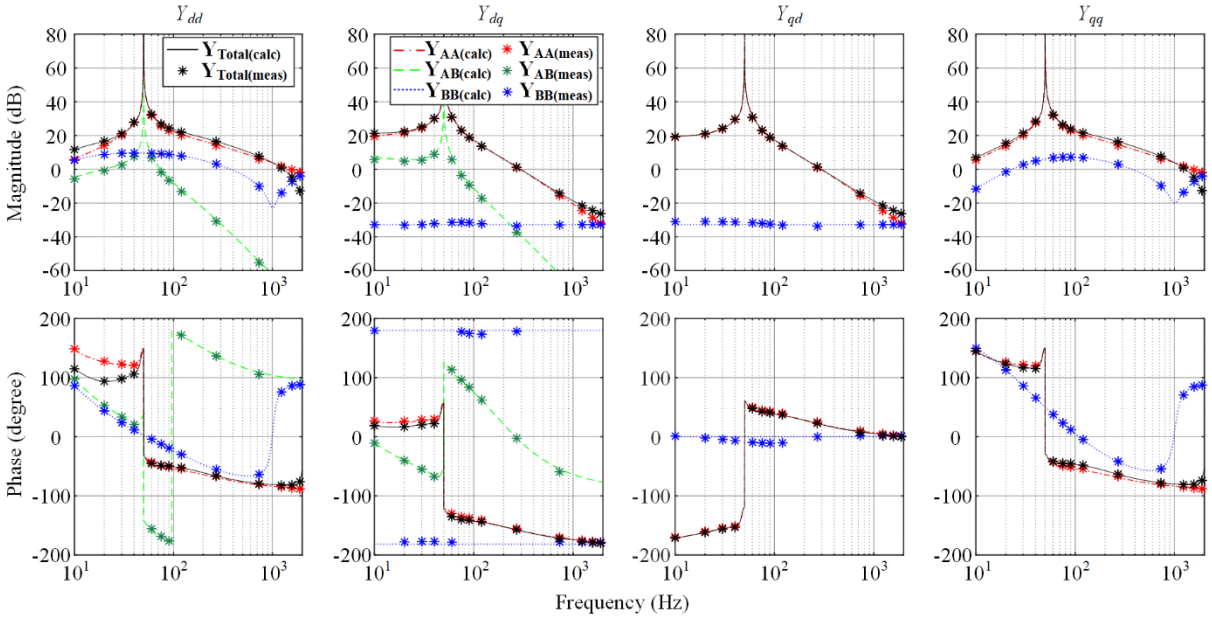

Fig. 6. Admittance measurement results of a GFM Type-3 wind generator under super-synchronous speed (ω_r = 60 Hz).

$$\mathbf{Y}_{\mathbf{BB}}^{\mathbf{dq}}(s) = (\mathbf{B}_{\mathbf{Lf}} + \mathbf{B}_{\mathbf{PI\text{-}I\text{-}2}} - \mathbf{B}_{\mathbf{PI\text{-}I\text{-}2}}\mathbf{B}_{\mathbf{PI\text{-}Vdc}} G_{Cdc} \mathbf{B}_{\mathbf{Vo\text{-}v}} - \mathbf{B}_{\mathbf{decpl\text{-}2}})^{-1} \cdot [\mathbf{I} - (\mathbf{B}_{\mathbf{PI\text{-}I\text{-}2}} - \mathbf{B}_{\mathbf{decpl\text{-}2}})\mathbf{B}_{\mathbf{pll\text{-}Ic}} - \mathbf{B}_{\mathbf{pll\text{-}Vc}} - \mathbf{B}_{\mathbf{PI\text{-}I\text{-}2}}\mathbf{B}_{\mathbf{PI\text{-}Vdc}} G_{Cdc} \mathbf{B}_{\mathbf{Vo\text{-}i}}] + \mathbf{B}_{\mathbf{Cf}} \quad (15)$$

where the detailed expressions of the matrixes are listed in (A13) - (A22) in the Appendix.

Overall, the admittance components $\mathbf{Y}_{\mathbf{AA}}$, $\mathbf{Y}_{\mathbf{AB}}$, $\mathbf{Y}_{\mathbf{BA}}$, and $\mathbf{Y}_{\mathbf{BB}}$ are obtained in (3), (10), (12), and (15). Then, the total admittance $\mathbf{Y}_{\mathbf{Total}}$ can also be obtained by adding the four admittance components $\mathbf{Y}_{\mathbf{AA}}$, $\mathbf{Y}_{\mathbf{AB}}$, $\mathbf{Y}_{\mathbf{BA}}$, and $\mathbf{Y}_{\mathbf{BB}}$.

IV. Simulation Verification

To verify the effectiveness of the proposed method, the simulation model of a 2 MW GFM Type-3 wind generator is built in Matlab/Simulink. The parameters of the DFIG and the RSC are listed in Table I and the parameters of the GSC are presented in Table II. In this section, the frequency scanning results and the calculated results of the terminal admittance will be provided for cross-validation.

TABLE I. PARAMETERS OF DFIG AND RSC

Parameters	Values
Rated phase voltage (peak value), V_{N1}	563 V (1 p.u.)
Rated angular frequency, ω_1	$2\pi \cdot 50$ rad/s (1 p.u.)
Rated active power of DFIG, P_{N1}	2 MW (1 p.u.)
Rotor speed, ω_r	40 ~ 60 Hz
Pole pairs, n_p	2
Stator resistance, R_s	1.7 mΩ (0.007 p.u.)
Rotor resistance, R_r	1.5 mΩ (0.006 p.u.)
Stator leakage inductance, $L_{\sigma s}$	0.038 mH (0.05 p.u.)
Rotor leakage inductance, $L_{\sigma r}$	0.064 mH (0.08 p.u.)
Mutual inductance, L_m	2.9 mH (3.83 p.u.)
Designed current-loop bandwidth, ω_{i1}	2000 rad/s
Virtual inductance, L_v	0.5 p.u.
Virtual resistance, R_v	0.05 p.u.
Cut-off angular frequency of LPFs, ω_{LPF}	300 rad/s
Active power droop coefficient, m_p	$2.5\% \cdot \omega_N/P_N$
Reactive power droop coefficient, n_q	$5\% \cdot V_N/P_N$

TABLE II. PARAMETERS OF GSC

Parameters	Values
Rated phase voltage (peak value), V_{N2}	563 V (1 p.u.)
Rated active power of GSC, P_{N2}	667 kW (1/3 p.u.)
Rated dc-link voltage, V_{dc}	1.1 kV
Dc-link capacitance, C_{dc}	10 mF
Filter inductance, L_f	0.34 mH
Filter resistance, R_f	3.6 mΩ
Filter capacitance, C_f	75 μF
Designed current-loop bandwidth, ω_{i2}	2000 rad/s
Damping ratio of dc voltage loop, ζ_{Vdc}	1
Natural frequency of dc voltage loop, ω_{nVdc}	40 rad/s
Damping ratio of PLL, ζ_{pll}	1
Natural frequency of PLL, ω_{npll}	200 rad/s

Same as [4], zero power condition is used in this paper for analysis. The d-q admittance measurement results by frequency scanning under sub-synchronous speed with ω_r = 40 Hz and super-synchronous speed with ω_r = 60 Hz are shown in Fig. 5 and Fig. 6 respectively, where the subscripts 'calc' and 'meas' denote calculation and measurement. Besides, the red, green, and blue curves show the d-q admittance characteristics of $\mathbf{Y_{AA}}$, $\mathbf{Y_{AB}}$, and $\mathbf{Y_{BB}}$ by calculation (i.e., equations (3), (10), and (15)). Since $\mathbf{Y_{BA}}$ is equal to 0, it is omitted in Fig. 5 and Fig. 6. Moreover, the black curves show the admittance characteristics of $\mathbf{Y_{Total}}$, which is equal to the sum of $\mathbf{Y_{AA}}$, $\mathbf{Y_{AB}}$, $\mathbf{Y_{BA}}$ and $\mathbf{Y_{BB}}$.

It can be seen from Fig. 5 and Fig. 6 that the measured admittances are basically overlapped with the calculated admittances in both sub-synchronous speed and super-synchronous speed cases, which demonstrates the correctness of the proposed method.

In addition, it can be seen that the dc-link coupling has stronger impact in the low-frequency range, because the magnitude of $\mathbf{Y_{AB}}$ is relatively higher. However, compared to $\mathbf{Y_{AA}}$ and $\mathbf{Y_{BB}}$, the magnitude of $\mathbf{Y_{AB}}$ is lower. So, $\mathbf{Y_{AA}}$ and $\mathbf{Y_{BB}}$ have higher weights than $\mathbf{Y_{AB}}$ in the selected study case in this paper. It is worth mentioning that the conclusions may be different in other study cases (e.g., other DFIG systems with different power ratings or different control schemes). Nevertheless, with the proposed method, the weights of $\mathbf{Y_{AA}}$, $\mathbf{Y_{AB}}$, and $\mathbf{Y_{BB}}$ can be observed clearly by comparing the magnitudes of them, which is beneficial for the model reduction and simplification.

V. CONCLUSION

This paper proposes a decoupled two-port-network-based full-order small-signal impedance modeling method for Type-3 wind generators. With this method, the total ac terminal admittance can be decomposed into four admittance components, and each of them can be modeled independently. So, the complexity of the modeling process is degraded. Besides, each admittance component has a physical meaning (i.e., $\mathbf{Y_{AA}}$ represents the model of the RSC-side subsystem, $\mathbf{Y_{BB}}$ represents the model of the GSC-side subsystem, and $\mathbf{Y_{AB}}$ represents the model of the dc-link coupling.) Thus, the impact of the dc-link coupling can be analyzed quantitatively and intuitively. Compared with conventional approximate modeling methods, the proposed modeling method has higher accuracy, because all the information of the system can be captured. The admittance measurement results by simulation have verified the correctness of the proposed modeling method.

APPENDIX

The 2×2 matrixes in the impedance model shown in Fig. 2 are given by (A1) - (A22).

$$\mathbf{B_{PI\text{-}I\text{-}1}} = \begin{bmatrix} K_{p1} + K_{i1}/s & 0 \\ 0 & K_{p1} + K_{i1}/s \end{bmatrix} \tag{A1}$$

$$\mathbf{B_{decpl\text{-}1}} = \begin{bmatrix} 0 & -\omega_{slip}\sigma L_r \\ \omega_{slip}\sigma L_r & 0 \end{bmatrix} \tag{A2}$$

$$\mathbf{B_{Lv}} = \begin{bmatrix} sL_v + R_v & -\omega_1 L_v \\ \omega_1 L_v & sL_v + R_v \end{bmatrix} \tag{A3}$$

$$\mathbf{B_{Ls}} = \begin{bmatrix} sL_s & -\omega_1 L_s \\ \omega_1 L_s & sL_s \end{bmatrix} \tag{A4}$$

$$\mathbf{B_{Lm}} = \begin{bmatrix} sL_m & -\omega_{slip} L_m \\ \omega_{slip} L_m & sL_m \end{bmatrix} \tag{A5}$$

$$\mathbf{B_{Lr}} = \begin{bmatrix} s\sigma L_r + R_r & -\omega_{slip}\sigma L_r \\ \omega_{slip}\sigma L_r & s\sigma L_r + R_r \end{bmatrix} \quad \text{(A6)}$$

$$\mathbf{B_{Vs\text{-}i}} = \frac{3}{2}\begin{bmatrix} v_{sq0}i_{sd0} & v_{sq0}i_{sq0} \\ -v_{sd0}i_{sd0} & -v_{sd0}i_{sq0} \end{bmatrix} \quad \text{(A7)}$$

$$\mathbf{B_{Vs\text{-}v}} = \frac{3}{2}\begin{bmatrix} -v_{sq0}v_{sd0} & -v_{sq0}v_{sq0} \\ v_{sd0}v_{sd0} & v_{sd0}v_{sq0} \end{bmatrix} \quad \text{(A8)}$$

$$\mathbf{B_{Vr\text{-}i}} = \frac{3}{2}\begin{bmatrix} v_{rq0}i_{sd0} & v_{rq0}i_{sq0} \\ -v_{rd0}i_{sd0} & -v_{rd0}i_{sq0} \end{bmatrix} \quad \text{(A9)}$$

$$\mathbf{B_{Vr\text{-}v}} = \frac{3}{2}\begin{bmatrix} -v_{rq0}v_{sd0} & -v_{rq0}v_{sq0} \\ v_{rd0}v_{sd0} & v_{rd0}v_{sq0} \end{bmatrix} \quad \text{(A10)}$$

$$\mathbf{B_{Ir\text{-}i}} = \frac{3}{2}\begin{bmatrix} i_{rq0}i_{sd0} & i_{rq0}i_{sq0} \\ -i_{rd0}i_{sd0} & -i_{rd0}i_{sq0} \end{bmatrix} \quad \text{(A11)}$$

$$\mathbf{B_{Ir\text{-}v}} = \frac{3}{2}\begin{bmatrix} -i_{rq0}v_{sd0} & -i_{rq0}v_{sq0} \\ i_{rd0}v_{sd0} & i_{rd0}v_{sq0} \end{bmatrix} \quad \text{(A12)}$$

$$\mathbf{B_{PI\text{-}I\text{-}2}} = \begin{bmatrix} K_{p2} + K_{i2}/s & 0 \\ 0 & K_{p2} + K_{i2}/s \end{bmatrix} \quad \text{(A13)}$$

$$\mathbf{B_{decpl\text{-}2}} = \begin{bmatrix} 0 & -\omega_1 L_f \\ \omega_1 L_f & 0 \end{bmatrix} \quad \text{(A14)}$$

$$\mathbf{B_{Lf}} = \begin{bmatrix} sL_f + R_f & -\omega_1 L_f \\ \omega_1 L_f & sL_f + R_f \end{bmatrix} \quad \text{(A15)}$$

$$\mathbf{B_{PI\text{-}Vdc}} = \begin{bmatrix} -K_{p\_Vdc} - K_{i\_Vdc}/s & 0 \\ 0 & 0 \end{bmatrix} \quad \text{(A16)}$$

$$G_{Cdc} = \frac{1}{(C_{dc}/2)s} \quad \text{(A17)}$$

$$\mathbf{B_{Vo\text{-}v}} = \frac{3}{2}\begin{bmatrix} v_{od0} & v_{oq0} \\ 0 & 0 \end{bmatrix} \quad \text{(A18)}$$

$$\mathbf{B_{Vo\text{-}i}} = \frac{3}{2}\begin{bmatrix} i_{cd0} & i_{cq0} \\ 0 & 0 \end{bmatrix} \quad \text{(A19)}$$

$$\mathbf{B_{pll\text{-}Vc}} = \begin{bmatrix} 0 & -v_{cq0}\cdot G_{pll}/V_o \\ 0 & v_{cd0}\cdot G_{pll}/V_o \end{bmatrix} \quad \text{(A20)}$$

$$\mathbf{B_{pll\text{-}Ic}} = \begin{bmatrix} 0 & -i_{cq0}\cdot G_{pll}/V_o \\ 0 & i_{cd0}\cdot G_{pll}/V_o \end{bmatrix} \quad \text{(A21)}$$

$$\mathbf{B_{Cf}} = \begin{bmatrix} sC_f & -\omega_1 C_f \\ \omega_1 C_f & sC_f \end{bmatrix} \quad \text{(A22)}$$

REFERENCES

[1] "GC0137: Minimum specification required for provision of GB grid forming (GBGF) capability," *National Grid ESO*, UK, Dec. 2021.

[2] U. Markovic, O. Stanojev, P. Aristidou, E. Vrettos, D. Callaway and G. Hug, "Understanding small-signal stability of low-inertia systems," *IEEE Trans. Power Syst.*, vol. 36, no. 5, pp. 3997-4017, Sep. 2021.

[3] L. Huang, C. Wu, D. Zhou, F. Blaabjerg, "A power-angle-based adaptive overcurrent protection scheme for grid-forming inverter under large grid disturbances", *IEEE Trans. Ind. Electron.*, vol.70, no.6, pp.5927-5936, 2023.

[4] R. Rosso, X. Wang, M. Liserre, X. Lu and S. Engelken, "Grid-forming converters: control approaches, grid-synchronization, and future trends - A review," *IEEE Open J. Ind. Appl.*, vol. 2, pp. 93-109, 2021.

[5] L. Huang, C. Wu, D. Zhou and F. Blaabjerg, "Impact of virtual admittance on small-signal stability of grid-forming inverters," *6th IEEE Workshop Electron. Grid (eGRID)*, New Orleans, LA, USA, 2021, pp. 1-8.

[6] L. Huang, C. Wu, D. Zhou, L. Chen, D. Pagnani, and F. Blaabjerg. "Challenges and potential solutions of grid-forming converters applied to wind power generation system—An overview." *Front. Energy Res.*, vol. 11, p. 1040781, 2023.

[7] A. Kushwaha and I. Singh, "Literature review paper on doubly fed induction generator wind turbine technology," *Int. J. Enh. Res. Sci. Tech. Eng.*, vol. 2, no. 9, pp. 44-50, Sep. 2013.

[8] J. L. Rodríguez-Amenedo, S. A. Gómez, J. C. Martínez and J. Alonso-Martinez, "Black-start capability of DFIG wind turbines through a grid-forming control based on the rotor flux orientation," *IEEE Access*, vol. 9, pp. 142910-142924, 2021.

[9] L. Huang, H. Xin, L. Zhang, Z. Wang, K. Wu and H. Wang, "Synchronization and frequency regulation of DFIG-based wind turbine generators with synchronized control," *IEEE Trans. Energy Conv.*, vol. 32, no. 3, pp. 1251-1262, Sept. 2017.

[10] I. Oraa, J. Samanes, J. Lopez and E. Gubia, "Modeling of a droop-controlled grid-connected DFIG wind turbine," *IEEE Access*, vol. 10, pp. 6966-6977, 2022.

[11] J. Hu, Y. Huang, D. Wang, H. Yuan and X. Yuan, "Modeling of grid-connected DFIG-based wind turbines for DC-link voltage stability analysis". *IEEE Trans. Sust. Energy*, vol. 6, no. 4, pp. 1325-1336, Oct. 2015.

[12] Y. Xu, H. Nian, T. Wang, L. Chen and T. Zheng, "Frequency coupling characteristic modeling and stability analysis of doubly fed induction generator," *IEEE Trans. Energy Conv.*, vol. 33, no. 3, pp. 1475-1486, Sep. 2018.

[13] I. Vieto and J. Sun, "Sequence impedance modeling and analysis of Type-III wind turbines," *IEEE Trans. Energy Conv.*, vol. 33, no. 2, pp. 537-545, Jun. 2018.

[14] C. Zhang, X. Cai, M. Molinas and A. Rygg, "Frequency-domain modelling and stability analysis of a DFIG-based wind energy conversion system under non-compensated AC grids: impedance modelling effects and consequences on stability," *IET Power Electron.*, vol. 12, no. 4, pp. 907-914, Apr. 2019.

[15] J. Sun and I. Vieto, "Development and application of Type-III turbine impedance models including DC bus dynamics," *IEEE Open J. Power Electron.*, vol. 1, pp. 513-528, 2020.

[16] S. Shah and V. Gevorgian, "Control, operation, and stability characteristics of grid-forming Type III wind turbines," National Renew. Energy Lab. (NREL), Golden, CO, USA, pp. 1-7, 2020.